AGU100 ADVANCING EARTH AND SPACE SCIENCE

JGR Space Physics

RESEARCH ARTICLE
10.1029/2018JA026434

Formation of Plasma Around a Small Meteoroid: Electrostatic Simulations

G. Sugar[1], M. M. Oppenheim[2], Y. S. Dimant[2], and S. Close[1]

[1]Department of Aeronautics and Astronautics, Stanford University, Stanford, CA, USA, [2]Center for Space Physics, Boston University, Boston, MA, USA

Key Points:
- We model the plasma density formed around a small ablating meteoroid with particle-in-cell simulations
- The simulations relax assumptions used in previous solutions by including charged particle dynamics as well as electric and magnetic fields
- Electric and magnetic fields have little effect on the ion distribution but do impact the electron distribution

Correspondence to:
G. Sugar,
gsugar@stanford.edu

Citation:
Sugar, G., Oppenheim, M. M., Dimant, Y. S., & Close, S. (2019). Formation of plasma around a small meteoroid: Electrostatic simulations. *Journal of Geophysical Research: Space Physics*, *124*. https://doi.org/10.1029/2018JA026434

Received 23 DEC 2018
Accepted 19 APR 2019
Accepted article online 1 MAY 2019

Abstract Obtaining meteoroid mass from head echo radar cross section depends on the assumed plasma density distribution around the meteoroid. An analytical model presented in Dimant and Oppenheim (2017a, https://doi.org/10.1002/2017JA023960; 2017b, https://doi.org/10.1002/2017JA023963) and simulation results presented in Sugar et al. (2018, https://doi.org/10.1002/2018JA025265) suggest the plasma density distribution is significantly different than the spherically symmetric Gaussian distribution used to calculate meteoroid masses in many previous studies. However, these analytical and simulation results ignored the effects of electric and magnetic fields and assumed quasi-neutrality. This paper presents results from the first particle-in-cell simulations of head echo plasma that include electric and magnetic fields. The simulations show that the fields change the ion density distribution by less than ~ 2% in the meteor head echo region, but the electron density distribution changes by up to tens of percent depending on the location, electron energies, and magnetic field orientation with respect to the meteoroid path.

1. Introduction

When a meteoroid enters the Earth's atmosphere, collisions with atmospheric molecules heat the meteoroid's surface. Neutral particles ablate from the meteoroid surface once the surface temperature reaches the sublimation point of the constituent materials. These ablated particles experience high-energy collisions with atmospheric particles and can ionize, creating a dense plasma around the meteoroid. High-power large-aperture (HPLA) radars, such as the Jicamarca Radio Observatory, ALTAIR, and the Arecibo Observatory, detect this plasma as a head echo (Chau & Woodman, 2004; Close et al., 2002; Janches & Revelle, 2005).

HPLA radars can detect multiple head echoes a second, enabling the collection of a vast data set of head echoes to better understand meteoroid properties such as mass, density, and composition. However, it is vital to have an accurate model of the plasma that produces a head echo in order to estimate such properties. Previous studies that use head echoes to calculate meteoroid mass assume a spherically symmetric Gaussian plasma distribution (Campbell-Brown et al., 2012; Close et al., 2005; Dyrud & Janches, 2008; Zinn et al., 2011). However, this distribution has not been validated by analytical or empirical evidence. Marshall et al. (2017) shows that the choice of the plasma distribution shape can cause the calculated electron line density (and therefore the meteoroid mass) to change by a factor of 3 for a head echo with a set radar cross section (RCS). This is a large source of error and demonstrates the necessity for a validated head echo plasma density model.

A recently proposed analytical model, hereinafter referred to as the Dimant-Oppenheim model or the DO model, validated with numerical simulations suggests a more complex and spherically asymmetric plasma distribution than the spherically symmetric Gaussian distributions used in the past (Dimant & Oppenheim, 2017a, 2017b; Sugar et al., 2018). However, the DO model assumes that electric and magnetic fields have a negligible effect on the ion motion and can be ignored. This paper relaxes that assumption and presents particle-in-cell (PIC) simulations to study the effects of electric and magnetic fields on the head echo plasma. The DO model also assumes quasi-neutrality, thereby approximating the electron distribution with the ion distribution. Simulations presented in this paper do not assume quasi-neutrality and track electrons and ions separately.

The results presented in this paper, as well as the DO model, describe the head echo region of a meteor and not the meteor trail. The head echo region contains dense plasma that travels with the parent meteoroid,

while the trail consists of a less dense plasma that remains in the wake of the meteoroid. Because the head echo moves with the meteoroid, it is limited to a small region of a few λ_T, the average distance an ablated particle travels from the meteoroid before colliding with an atmospheric molecule,

$$\lambda_T = \frac{V_T}{n_A \sigma U}, \tag{1}$$

where V_T is the thermal velocity of the ablated neutral atoms, n_A is the atmospheric number density, σ is the collisional cross section, and U is the meteoroid speed. Beyond a few λ_T, an ablated particle has a significantly different velocity than the parent meteoroid due to momentum exchanging collisions with the background atmosphere and will generally be significantly behind the meteoroid rather than in the head echo region. For the purposes of this paper, we define the head echo region (or near-meteoroid region) to be within $3\lambda_T$ of the meteoroid center because the vast majority of ablated particles beyond $3\lambda_T$ would have experienced multiple collisions with atmospheric particles and therefore have significantly different velocities than the meteoroid.

This paper is organized as follows. First we will discuss the methods used to numerically determine the plasma density distribution around an ablating meteoroid. Second, we will show simulation results and investigate how different boundary conditions, electron energy models, and magnetic field orientations affect the ion and electron distributions, as well as how the simulation results compare to the DO model. Finally, we will conclude with a discussion of the results and future work to investigate the potential impact on meteoroid mass estimates.

2. Simulations

We used the Electrostatic Parallel Particle-in-Cell simulator (EPPIC) to run our simulations using the Stampede2 system accessed through XSEDE (Oppenheim et al., 2008; Oppenheim & Dimant, 2013; Towns et al., 2014). EPPIC is a standard electrostatic PIC simulator: Charge density is calculated on a grid over the simulation domain; the potential at each grid point is calculated via Poisson's equation,

$$\nabla^2 \phi = -\frac{\rho}{\epsilon_0}, \tag{2}$$

where ϕ is the potential, ρ is the charge density, and ϵ_0 is the permittivity of free space; the electric field, $\vec{E}$, is calculated at each particle's position; and each particle's velocity, $\vec{v}$ is updated using the Lorentz force,

$$\overrightarrow{\Delta v} = \frac{q}{m}\left(\vec{E} + \vec{v} \times \vec{B}\right) \Delta t, \tag{3}$$

where m is the particle mass, q is the particle charge, $\vec{B}$ is the magnetic field, and Δt is the simulation time step. Finally, each particle's position, $\vec{r}$, is updated using

$$\overrightarrow{\Delta r} = \vec{v} \Delta t. \tag{4}$$

EPPIC also includes collision physics, allowing velocity changes as well the creation of ions and electrons in the event of ionizing collisions. Collisions are described in detail in section 2.4.

2.1. Parameters

The simulations track three types of particles: ablated meteoroid neutrals, electrons, and ions. The electron mass is set to 10 times the real electron mass to reduce the computational cost of simulations. Artificially increasing the electron mass is a typical method used in PIC codes to resolve both ion and electron dynamics in a single simulation (Bret & Dieckmann, 2010). Each simulation particle represents 2,000 real particles. The background atmospheric neutrals are not modeled as individual particles but rather as a constant uniform density of n_A. This model is valid because both the simulation domain size and the distance the meteoroid will travel during the simulation duration are much less than the scale height of the atmosphere at 100 km, the chosen altitude for the simulation.

We cannot simulate the complete life of the meteor as it moves through the entire ablation region of the atmosphere (120–75 km) because that would require unfeasible amounts of computation time. We therefore chose to find the steady state plasma distribution around the meteoroid at 100-km altitude, where n_A is

Table 1
Simulation Parameters

Parameter	Value	Units
Simulation electron mass (m_e)	9.1×10^{-30}	kg
Simulation ion mass (m_i)	3.8×10^{-26}	kg
Magnetic field ($\vec{B}$)	$4.0 \times 10^{-5}\hat{x}$	T
Elementary charge (q)	1.6×10^{-19}	C
Grid ($n_x \times n_y \times n_z$)	$512 \times 512 \times 512$	points
Grid size ($\Delta x = \Delta y = \Delta z$)	0.005	m
Time step (Δt)	2×10^{-8}	s
Atmospheric number density (n_A)	10^{19}	m^{-3}
Atmospheric particle (N_2) mass (m_A)	4.7×10^{-26}	kg
Ionosphere plasma density (n_I)	1.9×10^{9}	m^{-3}
Ionosphere electron thermal velocity ($V_{T_{Ie}}$)	1.96×10^{4}	m/s
Ionosphere ion thermal velocity ($V_{T_{Ii}}$)	303.4	m/s
Meteoroid speed (U)	40,000	m/s
Meteoroid radius (r_m)	1×10^{-4}	m
Ablated particle thermal velocity (V_{Tm})	951	m/s
Ablated particle (Na) mass (m_m)	3.8×10^{-26}	kg
Ablation rate (C)	2.5×10^{10}	simulation particles/s

approximately 10^{19} m^{-3}. The simulation is in the meteoroid's frame of reference, so atmospheric particles are moving at $-\vec{U} = 40\hat{z}$-km/s velocity.

The choice of using 100-km altitude and 40 km/s is based off typical values for meteor head echoes. A study using the Arecibo Observatory found that typical meteor head echoes moving at 40-km/s velocity are initially observed between 101- and 111-km altitude (Figure 9b in Janches et al., 2003). Head echoes typically span about 10 km in altitude making the observable range of 40 km/s about 91–111 km, so 100-km altitude is a reasonable choice for simulating a 40-km/s meteor head plasma. However, the results can be scaled to arbitrary altitudes and meteoroid velocities by appropriately scaling λ_T. The scaling might not be perfect because the ratio of the neutral-neutral and ion-neutral collision rates may change slightly as a function of altitude and meteoroid velocity. These changes can create quantitative but not qualitative differences.

The simulation uses a Cartesian coordinate system defined as follows (unless otherwise specified): $\hat{z}$ points along the meteoroid path behind the meteoroid, $\hat{x}$ points in the direction of the magnetic field, and $\hat{x} \times \hat{y} = \hat{z}$. The above and other critical simulation parameters are shown in Table 1.

2.2. Initialization

The simulation is initialized with a nighttime ionosphere at 100-km altitude by placing relatively cold (380 K) and low-density ($n_I = 1.9 \times 10^9$ m^{-3}) ions and electrons in the domain. The particle positions are sampled from a uniform random distribution, and the ith velocity component, V_i, is sampled from a Gaussian distribution:

$$V_i \sim \frac{1}{\sqrt{2\pi} V_{T_{Ip}}} e^{-\frac{(V_i - V_{di})^2}{2V_{T_{Ip}}^2}}, \tag{5}$$

where V_{di} is the drift velocity component in the ith direction, and $V_{T_{Ip}}$ is the ionospheric thermal velocity for a particle (either an electron [$V_{T_{Ie}}$] or ion [$V_{T_{Ii}}$]), constant in all directions. The subscript $_I$ is used to distinguish between ionospheric charged particles and charged particles resulting from ionizing collisions. We model the meteoroid as a spherically symmetric source of ablated neutral particles placed at the origin with radius r_m and creation rate C.

We do not expect changes in r_m to affect the plasma distribution as long as r_m is significantly smaller than the grid spacing (Δx) because the spherical source of ablated neutral particles will appear as a point source in the simulation domain if $r_m \ll \Delta x$. Studies have shown that the vast majority of head echoes observed

by HPLA radars are below 10^{-7} kg (Close et al., 2005, 2007). Assuming a spherical meteoroid and a density of 1 g/cm^3, a 10^{-7}-kg meteoroid will have an $r_m = 2.88 \times 10^{-4}$ m, significantly less than the grid spacing of 5×10^{-3} m used in the simulations.

2.3. Boundary Conditions

There are two types of boundary conditions to consider. The first is a particle boundary, which determines what happens to a particle that crosses a domain boundary, and the second is a field boundary, which specifies the boundary conditions used when solving for the potential (equation (2)). The simulation uses both periodic and open particle boundaries. Particles that cross a periodic boundary are injected at the opposite side, while particles that cross an open boundary are deleted. At every open boundary there is a constant stream of particles injected into the domain to simulate the ionosphere plasma outside of the simulation domain. The number of particles to inject, N, at each time step is

$$N = A\Phi\Delta t, \tag{6}$$

where A is the area of the injection boundary, and Φ is the flux of particles entering the domain through the boundary. An injected particle's position on the injection plane is sampled from a uniform random distribution and then is advanced by a time step of $a\Delta t$, where a is a random number sampled from a uniform distribution between $[0, 1]$. The particle's velocity components parallel to the injection plane are sampled from a Gaussian distribution (equation (5)), and the velocity component perpendicular to the injection plane, $V_\perp$, is sampled from a Gaussian flux distribution,

$$V_\perp \sim \frac{V_\perp}{V_{TIp}\left(\sqrt{\frac{\pi}{2}}V_{d\perp}\left(1+\mathrm{erf}\left(\frac{V_{d\perp}}{\sqrt{2}V_{TIp}}\right)\right)+V_{TIp}e^{\frac{-V_{d\perp}^2}{2V_{TIp}^2}}\right)}e^{-\frac{\left(V_\perp - V_{d\perp}\right)^2}{2V_{TIp}^2}}, \tag{7}$$

where $V_{d\perp}$ is the drift velocity component in the direction perpendicular to the boundary, and erf is the error function. The perpendicular velocity component must be sampled from a Gaussian flux rather than a Gaussian distribution because more particles with high perpendicular velocity components will cross the boundary than particles with low perpendicular velocity components in a single time step. For example, if V_T was sampled from a Gaussian distribution, then there would be some particles injected with a 0 perpendicular velocity component. However, a particle with a 0 perpendicular velocity component would never cross the injection plane and therefore should not be injected into the domain. Sampling $V_\perp$ from a Gaussian flux distribution solves this problem and gives the correct result.

Given unlimited computational resources, a meteor head echo plasma would be best modeled with all open particle boundaries. However, periodic particle boundaries improve the simulation speed and do not drastically affect the near-meteoroid results if the periodic boundary planes are parallel to the meteor path ($\hat{z}$) and sufficiently far from the meteoroid center. For this reason, only the $\pm\hat{z}$ particle boundaries are open and the $\pm\hat{x}$ and $\pm\hat{y}$ boundaries are periodic and placed $15.79\lambda_T$ from the meteoroid center. This models multiple meteors moving in parallel at a distance of $31.58\lambda_T$ from each other. Because the boundaries are far away from the meteoroid and the atmospheric neutrals are moving fast in the $\hat{z}$ direction, a particle originating in the near-meteoroid region that travels across a periodic boundary will experience many collisions and be far behind the near-meteoroid region. Therefore, we consider the periodic $\pm\hat{x}$ and $\pm\hat{y}$ particle boundaries to be sufficiently far away from the meteoroid and they should not have significant impact on the near-meteoroid region. We explore the effects of changing the domain size in section 3.2.

The field boundaries are assigned as follows. Boundaries normal to $\hat{z}$ (the meteoroid path) are set to either Neumann ($\nabla\phi_{BC} = 0$), Dirichlet, ($\phi_{BC} = 0$), or periodic conditions. Boundaries normal to $\hat{x}$ and $\hat{y}$ are always periodic in order to use a fast spectral field solver along the x and y dimensions. To most closely replicate a meteor, all field boundaries should be nonperiodic, but fully nonperiodic 3-D solvers require an order of magnitude more computation time than the partially nonperiodic spectral solvers. We explore the field boundary condition effects on the near-meteoroid results in section 3.3.

2.4. Collisions

The simulations track three types of particles: ablated meteoroid neutral particles, ions, and electrons, all of which experience collisions with the background neutral atmospheric particles (denoted as $n-n$, $i-n$, and

$e-n$, respectively). We do not include collisions between the tracked particles themselves because collisions with background atmospheric particles are much more frequent due to the over 5 orders of magnitude higher atmospheric particle density. The collision probability, P_{coll}, of any tracked particle with an atmospheric neutral in a time step is

$$P_{\text{coll}} = 1 - \exp(-n_A \sigma V_{\text{rel}} \Delta t), \tag{8}$$

where σ is the collisional cross section and V_{rel} is the relative velocity magnitude of the particle and the background atmosphere.

As in Dimant and Oppenheim (2017a, 2017b), all *i*-*n* and *n*-*n* collisions are treated as elastic collisions. Even though *n*-*n* collisions are often ionizing, the energy in a collision is typically $\sim$ 200 eV, while the ionization energy is much less ($\sim$ 5 eV for Na). Therefore, only a small percentage of the total collisional energy will be lost to ionization.

Similar to Sugar et al. (2018), we use the popular Bronshten (1983) collision cross section model for both *n*-*n* and *i*-*n* collisional cross sections,

$$\sigma_{in} = \sigma_{nn} = 5.61 \times 10^{-19} V_{\text{rel}}^{-0.8}, \tag{9}$$

where V_{rel} is the relative velocity between the colliding particles in kilometers per second and σ is the collisional cross section in square meters. This is admittedly a crude model with two potential issues. First, it is likely that $\sigma_{in} > \sigma_{nn}$ due to a higher ion-neutral interaction potential at far distances. Second, the difference between σ_{in} and σ_{nn} likely changes with collision velocity since σ is dependent on the relative velocity of the colliding particles. We resolve these issues by noting that once the relative speed of colliding particles is significantly different from the meteoroid speed, the colliding particles move behind the meteoroid and are not considered part of the head echo because the head echo moves with the meteoroid. Therefore, we are only concerned with accurately modeling σ_{in} and σ_{nn} for a small range of velocities centered around the meteoroid velocity. Analysis in section 5.3 of Sugar et al. (2018) uses Lennard-Jones interaction potential models for N_2 to show that σ_{in} and σ_{nn} are equal to within 1% for the relevant collision energies, supporting the $\sigma_{in} \approx \sigma_{nn}$ assumption.

To determine whether an *n*-*n* collision will be ionizing rather than a simple momentum transfer collision, we use the ionization probability model for Na in Vondrak et al. (2008):

$$\beta = 0.933(V_{\text{rel}} - 8.86)^2 V_{\text{rel}}^{-1.94}, \tag{10}$$

where β is the probability the collision is ionizing and V_{rel} again has units of kilometers per second. Meteor spectra show that singly ionized particles dominate meteor plasma, so we assume no *i*-*n* collisions are ionizing (Ceplecha et al., 1998).

In the event of an *n*-*n* ionizing collision, we assume that the ablated meteoroid particle is ionized rather than the atmospheric particle due to the lower ionization energy of Na compared to N_2. The simulation deletes the ablated neutral particle and creates an Na^+ ion and an electron at the collision location. We assume an elastic scattering model to set the ion velocity, while the electron velocity direction and magnitude in the center of mass frame are sampled from a random uniform distribution and a Gaussian distribution with standard deviation equal to 1 eV, respectively. The choice of a sampling from a 1-eV Gaussian distribution comes from work by Berry (1961) that studies the energy distribution of electrons originating from neutral heavy particle ionizing collisions. Figure 4 of Berry (1961) shows electron energy distributions for neutral Argon-Argon collisions with collision energies ranging from 300 to 3,000 eV. The distributions are similar over all collisional energy ranges, with approximately Gaussian electron energy distributions with standard deviation of $\sim$ 1 eV and slightly fatter tails than expected for a Gaussian. We explore the effect of different electron energy distributions in section 3.4.

Electron-neutral collisions are significantly different from *i*-*n* and *n*-*n* collisions. Experimental and theoretical results shown in Figure 7 of Frost and Phelps (1962) show the elastic collisional rates of electrons and N_2 are orders of magnitude smaller than inelastic collision rates for 0.001–1 eV electron energies. Therefore, we model the energy loss of inelastic collisions using the method outlined in Oppenheim et al. (2008) and Oppenheim and Dimant (2013), where electrons experience elastic collisions with neutrals that are a factor of 50 less massive than the actual neutral particle. The *e*-*n* collisional cross section is determined from lin-

early interpolating the electron-N_2 collisional cross section curve reported in Figure 6 of Frost and Phelps (1962).

The collision models discussed above drive much of the physics in the simulation, and it is important to note that there are many different models for collisional cross sections such as Lennard-Jones 12-6 potential models and Maxwell molecule collisions (Bouanich, 1992; Schunk & Nagy, 2004). We found that some of these models change σ by up to a factor of 4, which impacts λ_T and has the net effect of changing the spatial scale of the simulation with little impact on the characteristic shape of the ion and election distributions. Because there is a reasonably high uncertainty in σ (and therefore λ_T), any attempt to use the plasma distributions for meteoroid mass estimates should fit λ_T to radar data similar to how Marshall et al. (2017) fit the characteristic length parameter, r_0, of various plasma density distributions to head echoes using simultaneous triple-frequency radar observations.

2.5. External Electric Field

The simulation domain is in the meteoroid's frame of reference, but the magnetic field lines are stationary with respect to the Earth. Therefore, the magnetic field lines are moving with respect to the simulation domain's frame of reference. The moving magnetic field, $\vec{B}$, produces an background electric field, $\vec{E'}$, that can be calculated using the Lorentz transformation:

$$\vec{E'} = \gamma\left(\vec{E} - \vec{V}_B \times \vec{B}\right) - (\gamma - 1)\left(\vec{E} \cdot \hat{V}_B\right)\hat{V}_B, \tag{11}$$

where $\vec{V}_B$ is the magnetic field velocity in the meteoroid frame and γ is the Lorentz factor,

$$\gamma = \frac{1}{\sqrt{1 - \|\vec{V}_B\|^2/c^2}}, \tag{12}$$

where c is the speed of light. We assume there is no externally applied electric field in the Earth's frame of reference, so $\vec{E} = 0$. Also, the meteoroid is not moving at relativistic speeds, so $\gamma \approx 1$ and

$$\vec{E'} \approx -\vec{V}_B \times \vec{B}. \tag{13}$$

In the simulations, $\vec{V}_B = 4 \times 10^4 \hat{z}$ m/s and $\vec{B} = 4 \times 10^{-5} \hat{x}$ T, resulting in a net external field $\vec{E'} = -1.6\hat{y}$ V/m.

2.6. Length and Time Scales

To prevent numerical instabilities, the simulation should resolve relevant length and time scales: the gyroradii, gyrofrequency, plasma frequency, and Debye length. Also, particles should not cross more than one grid cell in a single time step on average.

The gyroradius, r_g, is calculated using

$$r_g = \frac{mV_\perp}{|q|B}, \tag{14}$$

where m is the particle mass, $V_\perp$ is the velocity component perpendicular to the magnetic field, q is the particle's charge, and B is the magnetic field magnitude. We assume a 40,000-nT magnetic field, which is within the range of reported values at 100-km altitude at midlatitudes (Chulliat et al., 2015). The particle population with the lowest gyroradii will have the lowest average $mV_\perp$, that is, the ionospheric electron population. Setting $V_\perp = V_{Tie}$ and $m = m_e$ results in $r_g = 0.0279$ m.

The gyrofrequency, ω_g, is calculated from

$$\omega_g = \frac{|q|B}{m}. \tag{15}$$

This gives an electron and ion gyrofrequency of 7.03×10^5 and 168 rad/s, respectively.

The plasma frequency,

$$\omega_p = \sqrt{\frac{n_e e^2}{m_e \epsilon_0}}, \tag{16}$$

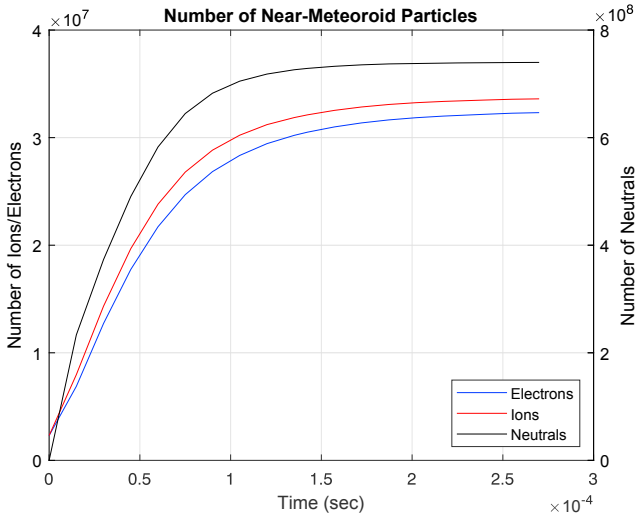

Figure 1. The number of simulation electrons (blue), ions (red), and ablated neutrals (black) in the near-meteoroid region as a function of time for the baseline simulation (Table 1 parameters with Neumann-Neumann $\hat{z}$ field boundaries). Ion and electron populations are on the left y axis, while neutrals correspond to the right y axis.

changes with the electron density and will be different in the background ionosphere and in the near-meteoroid region. The ionosphere plasma density (n_I) and electron mass (m_e) reported in Table 1 result in $\omega_p = 7.77\times10^5$ rad/s. In our simulations, the near-meteoroid region has a peak electron density of $\sim 10^{12}$ m^{-3} resulting in $\omega_p = 1.78\times10^7$ rad/s.

The Debye length, λ_D, is defined as

$$\lambda_D = \sqrt{\frac{kT_e\epsilon_0}{n_e q^2}}, \tag{17}$$

where k is Boltzmann's constant, and T_e is the electron temperature. Using $kT = (3/2)m_e V_T^2$, where V_T is the ionosphere electron thermal velocity (V_{TIe}), the ionosphere Debye length is 0.031 m. We approximate the minimum Debye length of the near-meteoroid region by taking the peak electron density ($\sim 10^{12}$ m^{-3}) and assuming 1-eV electrons. This results in a 0.0074-m Debye length, which is the smallest length scale we must resolve. Therefore, we set the grid cell size to $\Delta x = 0.005$ m.

To ensure most particles do not cross more than a single grid cell in a time step, we divide the grid cell size by the fastest expected particle velocity. The fastest particles will be the 1-eV electrons generated from the ionizing collisions, resulting in simulation electrons with 108-km/s velocities. If these electrons are also drifting with the background atmosphere, the time step must be less than 4.6×10^{-8} s in order to prevent the majority of electrons from crossing multiple grid cells in a time step. There will be some electrons with energies greater than 1 eV in the tail of the Gaussian velocity distribution, so we set the time step $\Delta t = 2\times10^{-8}$ s. This is the smallest time scale we must resolve and is adjusted accordingly when exploring the effects of higher electron energies in section 3.4.

3. Simulation Results

In this section we present the results from multiple simulations. First, we present evidence that the simulations reach a steady state in the near-meteoroid region ($r/\lambda_T < 3$). Second, we investigate domain sizing effects and show that the domain size is sufficient to obtain reliable results in the near-meteoroid region. The next subsections explore how different variables affect the head echo plasma by changing one variable at a time and comparing the results to a baseline simulation. The baseline simulation is run with the Table 1 parameters, $\vec{B} \perp \vec{U}$, and Neumann-Neumann field boundary conditions at the minimum and maximum z values. The final subsection compares the baseline simulation results to the analytical DO model.

3.1. Steady State

Because the simulation domain is significantly larger than the near-meteoroid region, achieving a steady state solution for the entire domain would take excessive amounts of computation time. Rather than achieving a steady state for the entire domain, we report the simulation results once an approximate steady state is achieved for the near-meteoroid region. Figure 1 shows the number of neutrals, ions, and electrons within the near-meteoroid region as a function of time. We consider a simulation to reach steady state once the number of near-meteoroid electrons changes by less than 0.03% in 1.5×10^{-5} s. This cutoff was chosen because the number of near-meteoroid particles is close to the asymptote and a consistent time is necessary to compare different simulations.

3.2. Domain Size

To ensure the simulation domain size is large enough to produce reliable results in the near-meteoroid region, we run three simulations of different domain sizes and see if steady state results converge as the domain size increases. Each simulation runs with the Table 1 parameters except with different n_x, n_y, and n_z. The "small" simulation has $n_x = n_y = n_z = 128$, a cube with $7.90\lambda_T$ sides; the "medium" simulation has $n_x = n_y = n_z = 256$, a cube with $15.79\lambda_T$ sides; and the "large" simulation has $n_x = n_y = n_z = 512$, a

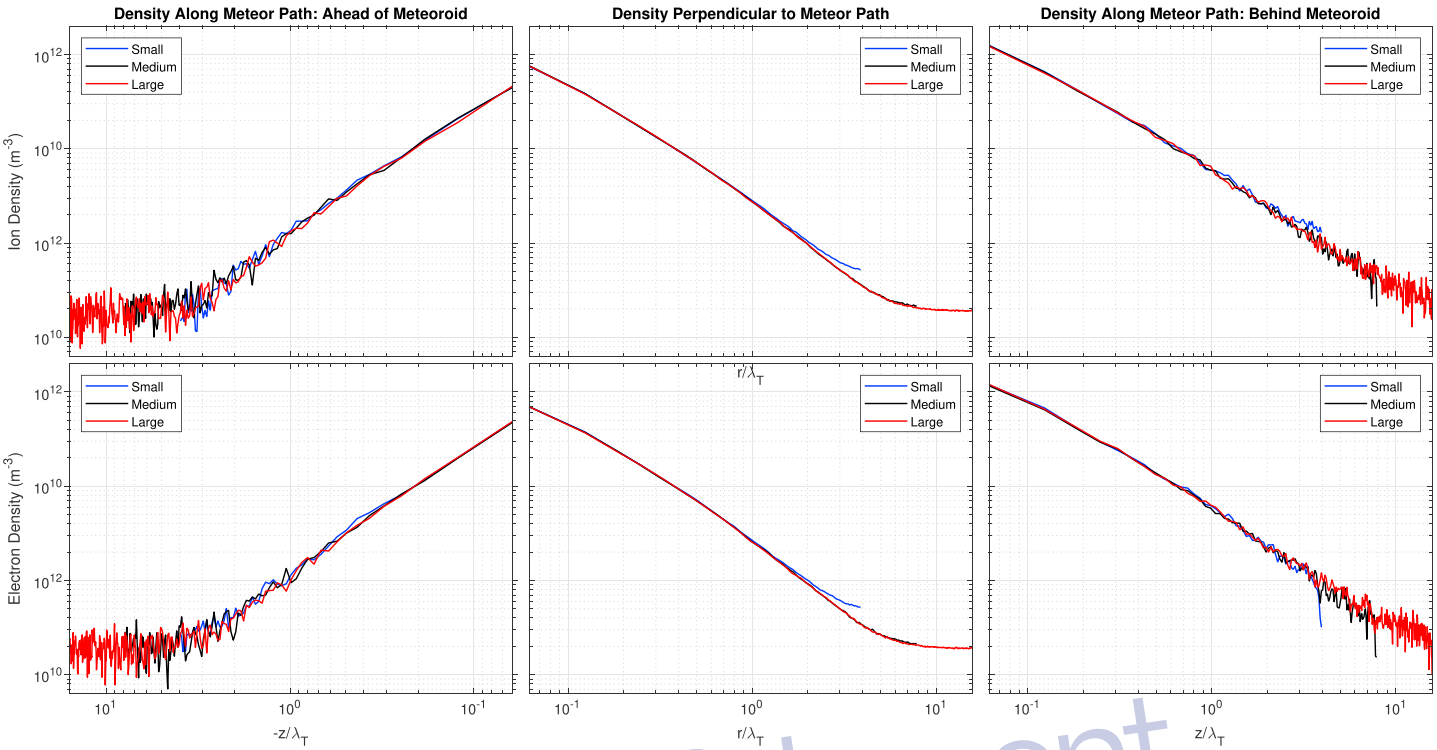

Figure 2. The ion (top row) and electron (bottom row) densities along three different contours for simulations with different domain sizes. The small, medium, and large domain results are in blue, black, and red, respectively. The left plots show densities on a contour along the meteoroid path ahead of the meteoroid, the middle plots show axially averaged (about the meteoroid path) densities on a contour perpendicular to the meteoroid path that passes through the meteoroid center, and the right plots show densities on a contour along the meteoroid path behind the meteoroid.

cube with $31.58\lambda_T$ sides. We expect the boundaries to significantly impact the ion and electron density distributions for the small simulation because the entire near-meteoroid region barely fits inside the domain. As explained in section 2.3, the periodic particle boundaries simulate an infinite number of meteors moving parallel to each other. If the boundaries are not sufficiently far from the meteoroid center, then the parallel meteor particle distributions will overlap and result in artificially high particle densities.

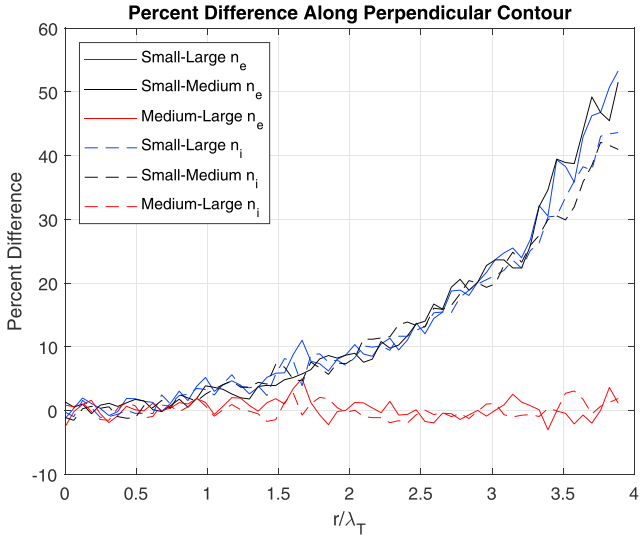

Figure 3. The percent difference between the small-large (blue), small-medium (black), and medium-large (red) sized simulations of electron densities (solid lines) and ion densities (dashed lines) along the perpendicular contour. The percent difference increases as distance to the boundary decreases for the small-large and small-medium lines, but not for the medium-large.

The boundary effects are apparent in Figure 2, which shows the ion (top row) and electron (bottom row) densities along three different contours for the three simulations. The three contours are as follows: along the meteor path ahead of the meteoroid (left plots), along a line perpendicular to the meteoroid path that passes through the meteoroid (middle plots), and along the meteoroid path behind the meteoroid (right plots). These three contours (ahead, perpendicular, and behind) will be used to explore the effects of other parameters in upcoming sections. The contours perpendicular to the meteor path show data that have been axially averaged about the meteor path. Even though the densities are not axially symmetric, the axial averaging is done to present a low-noise parameter for comparing different simulations. There are two main contributions to the noise, small number of PIC particles and small number of grid cells used to calculate the density. Each data point for the contours along the meteor path is calculated from a single grid cell, while the data points for the contour perpendicular to the meteor path are calculated from the axially averaged density at multiple grid cells. As r/λ_T increases along the perpendicular contour, more grid cells are used in the axial average. However, as z/λ_T increases for the contours along the meteor path, the density

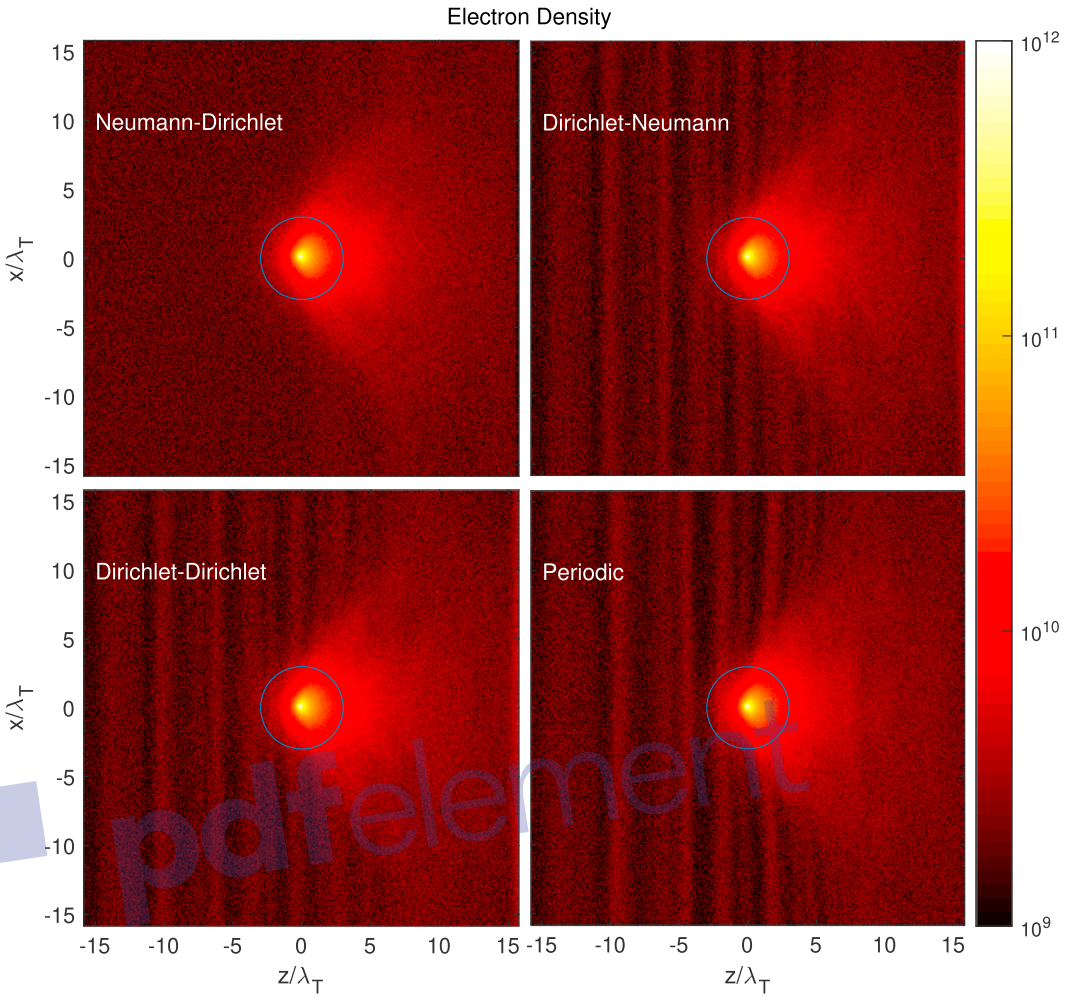

Figure 4. Electron densities in the xz plane for the Neumann-Dirichlet (top left), Dirichlet-Neumann (top right), Dirichlet-Dirichlet (bottom left), and periodic (bottom right) field boundary conditions. The near-meteoroid region ($r/\lambda_T < 3$) is inside the blue circle. Density values are in per cubic meter.

is still calculated from a single grid cell and the number of PIC particles decreases. This causes the noise to increase with distance from the meteoroid center for the contours along the meteor path (low number of particles and low number of grid cells) and the noise to remain small even at large distances from the meteoroid center for the perpendicular contour (low number of particles but large number of grid cells).

Figure 2 shows how the simulation results change with domain size and converge to a solution as the domain becomes larger. The left plots show little difference in ion and electron densities along the meteor path ahead of the meteoroid between the three simulations. This is likely due to the steep falloff in ion and electron density as the distance from the meteoroid increases in front of the meteoroid. At around $z/\lambda_t = -3$, the ion density approximately equals the ionosphere plasma density ($n_I = 1.9 \times 10^9$ m^3). However, the ion and electron densities are significantly higher than n_I for $r/\lambda_T > 2$ along the perpendicular contour (middle plots) and for $z/\lambda_T > 3$ behind the meteor (right plots). This suggests that the small domain boundaries are not sufficiently far away from the meteoroid center and there is significant overlap between the parallel meteor particle distributions in the half-space behind the meteor.

A clear trend of the error caused by a finite domain size is that the error increases as the distance to the boundaries decreases. This phenomenon can be seen in Figure 3, which shows the electron (solid lines) and ion (dashed lines) density percent difference between all combinations of the small, medium, and large simulations along the perpendicular contour (small-large difference in blue, small-medium difference in black, and medium-large difference in red). Because the boundaries significantly affect the small domain,

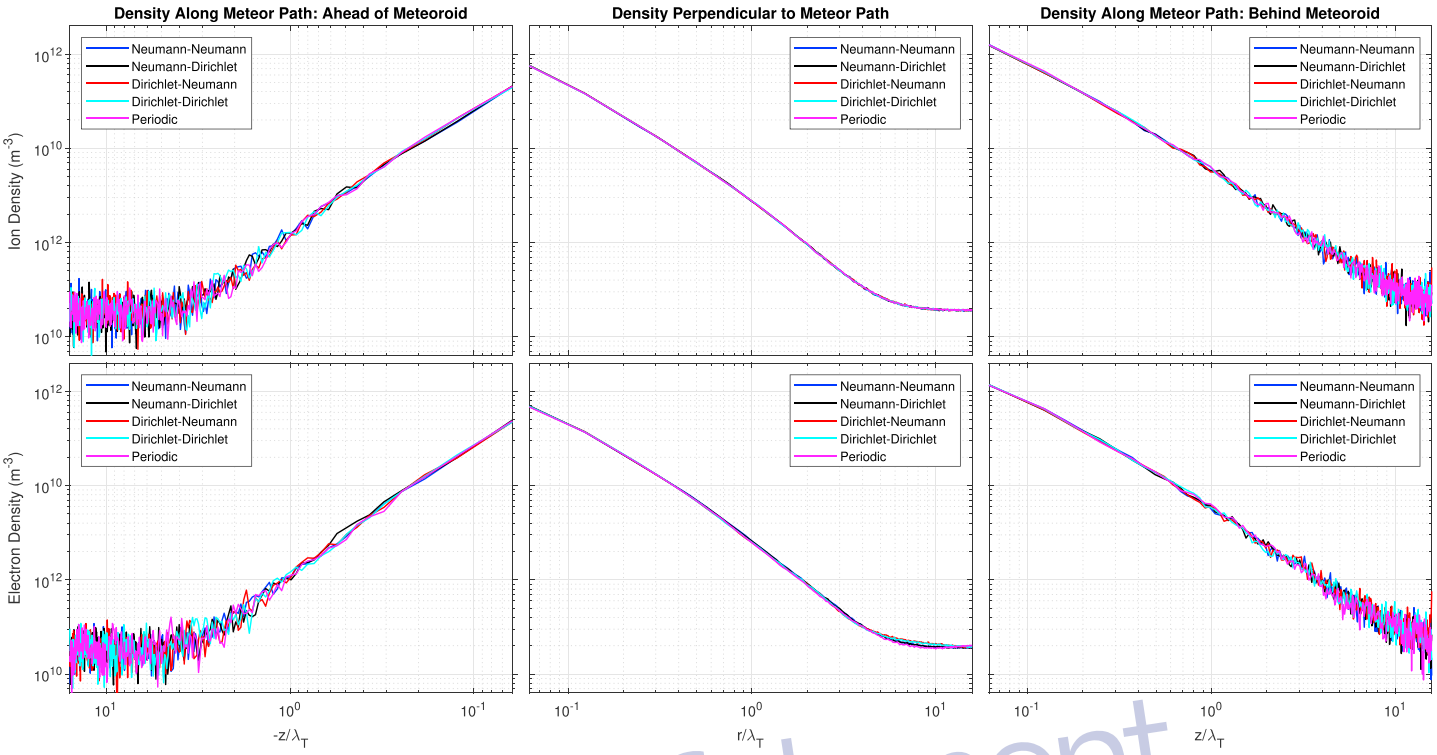

Figure 5. The ion (top row) and electron (bottom row) densities along three different contours for simulations with different boundary conditions along the two bounding planes perpendicular to the meteoroid path ($\hat{z}$). The Neumann-Neumann, Neumann-Dirichlet, Dirichlet-Neumann, Dirichlet-Dirichlet, and periodic results are in blue, black, red, cyan, and magenta, respectively. The left plots show densities on a contour along the meteoroid path ahead of the meteoroid, the middle plots show axially averaged (about the meteoroid path) densities on a contour perpendicular to the meteoroid path that passes through the meteoroid center, and the right plots show densities on a contour along the meteoroid path behind the meteoroid. Not all colors are visible on every plot because the different simulations produce similar densities and the lines are on top of each other.

the black and blue lines show increasing percent difference as r/λ_T approaches the boundary. The red lines do not show this trend, suggesting that the large simulation's size is sufficient for the boundaries to have negligible effect on the near-meteoroid region.

3.3. Field Boundary Effects

To investigate field boundary condition effects, we run five simulations with the same parameters outlined in Table 1 but using different boundary conditions on the two bounding planes perpendicular to the meteoroid path ($\hat{z}$). The bounding plane perpendicular to $\hat{z}$ in front of the meteoroid is called BP_+ and the bounding plane perpendicular to $\hat{z}$ behind the meteoroid is called BP_. The five different field boundary configurations are Neumann-Neumann ($\nabla\phi = 0$ on both BP_+ and BP_), Neumann-Dirichlet ($\nabla\phi = 0$ on BP_+ and $\phi = 0$ on BP_), Dirichlet-Neumann ($\phi = 0$ on BP_+ and $\nabla\phi = 0$ on BP_), Dirichlet-Dirichlet ($\phi = 0$ on both BP_+ and BP_), and periodic (ϕ_{xy} on $BP_+ = \phi_{xy}$ on BP_ for grid cells located at x, y). As stated in section 2.3, the other four bounding planes are periodic.

Figure 4 shows the electron density in the xz plane for the Neumann-Dirichlet (top left), Dirichlet-Neumann (top right), Dirichlet-Dirichlet (bottom left), and periodic simulations (bottom right). The Neumann-Neumann xz plane electron density is shown in Figure 11 third column, bottom plot and is very similar to the Neumann-Dirichlet plot. The ion distributions are not shown because they are similar across all five simulations. However, there are clear differences in the electron distributions between simulations with and without a Neumann BP_+ boundary. When the BP_+ boundary is allowed to have a nonzero E_z (i.e., a non-Neumann field boundary), a wave-like electron density structure is generated with wavefronts along $\hat{z}$ and can be seen in the Figure 4 top right plot and bottom plots.

These structures are likely due to a nonzero E_z along the boundary affecting the injected ionospheric electrons. As stated in section 2.3, electrons and ions are injected across the BP_+ and BP_ open particle boundaries and the injected particle flux is calculated assuming an unperturbed ionosphere. This assump-

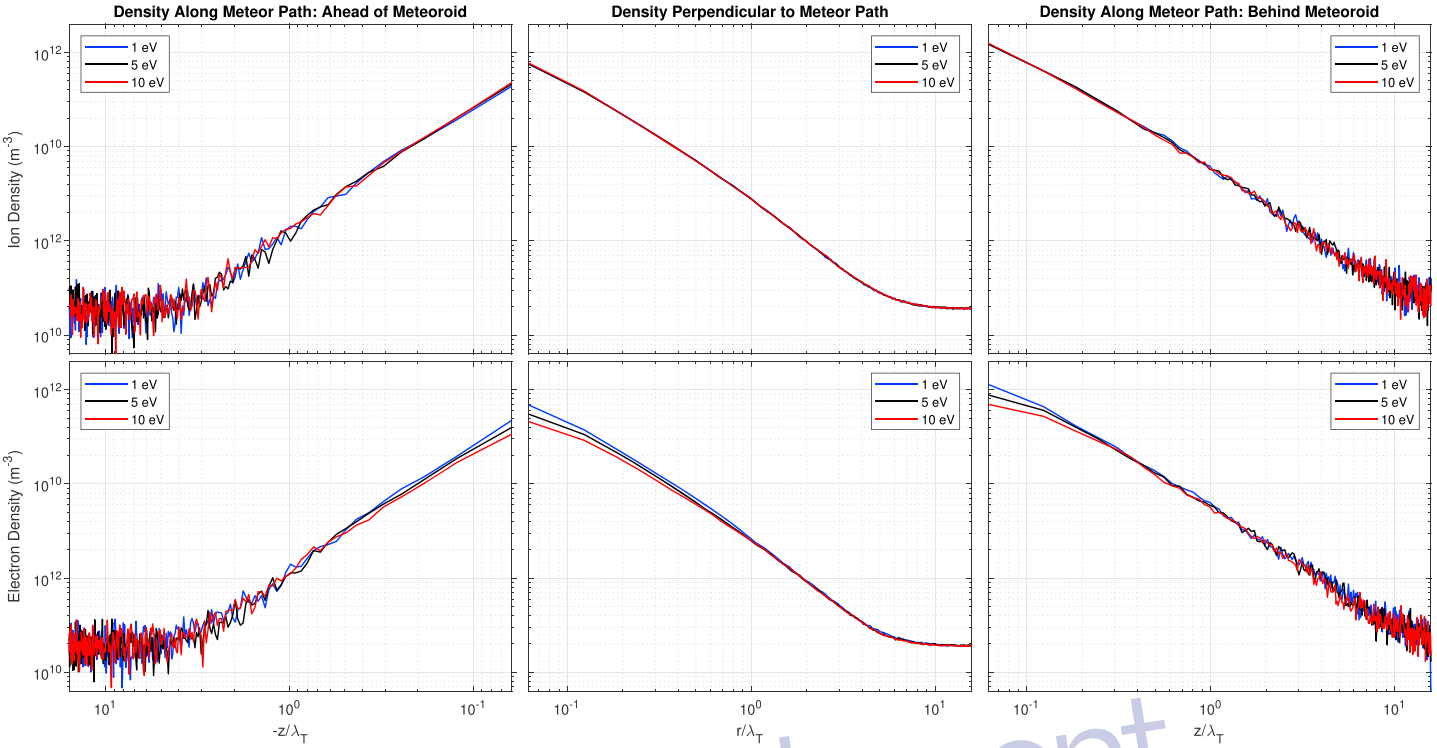

Figure 6. The ion (top row) and electron (bottom row) densities along three different contours for simulations using different electron energy models. The 1-, 5-, and 10-eV electron energy results are in blue, black, and red, respectively. The left plots show densities on a contour along the meteoroid path ahead of the meteoroid, the middle plots show axially averaged (about the meteoroid path) densities on a contour perpendicular to the meteoroid path that passes through the meteoroid center, and the right plots show densities on a contour along the meteoroid path behind the meteoroid.

tion is violated when there is a nonzero E_z at the boundary, causing an injection of an incorrect number of particles for non-Neumann BP_+ boundary conditions. The electron density wave structures are not seen in the Neumann-Dirichlet simulation even though there is a non-Neumann BP_ boundary because very few particles are injected across the BP_ boundary. The fast atmosphere velocity in the $\hat{z}$ direction causes the particle flux (Φ in equation (6)) into the domain across BP_ to be 2 orders of magnitude smaller than across BP_+.

While the field boundary conditions have a clear impact on the far-meteoroid region, they have relatively little impact on the near-meteoroid region. Figure 5 shows ion and electron densities along the front, perpendicular, and back contours for the different boundary condition simulations. The ion distributions are not significantly impacted by the boundary conditions, and the differences are within the noise. However, there are some slight differences outside of the noise in the electron distribution perpendicular contour (bottom middle plot). The Dirichlet-Neumann simulation has the largest percent difference with the baseline (Neumann-Neumann) simulation: 11.94% at $r/\lambda_T = 9.07$, which is far outside the near-meteoroid region. Inside the near-meteoroid region, the Dirichlet-Neumann simulation also has the largest percent difference with the baseline simulation, −7.79% at $r/\lambda_T = 2.90$. The electron density at $r/\lambda_T = 2.90$ is 2 orders of magnitude smaller than the peak electron density at the meteoroid center, so a −7.79% difference at $r/\lambda_T = 2.90$ will not have a significant impact on meteoroid mass determination assuming the difference has a negligible effect on the head echo RCS.

3.4. Electron Energies

We run three different simulations to explore the effect of the model used to assign electron energies after an ionizing collision. The three simulations use the Table 1 parameters, with the only difference being the energy model used to assign velocity to electrons created from ionizing collisions. The first simulation uses the 1-eV distribution described in section 2.4, the second uses a 5-eV distribution, and the third uses a 10-eV distribution. Figure 6 shows the ion (top row) and electron (bottom row) densities along the usual front, perpendicular, and back contours, and Figure 7 shows the charge density on a zoomed in portion of the yz

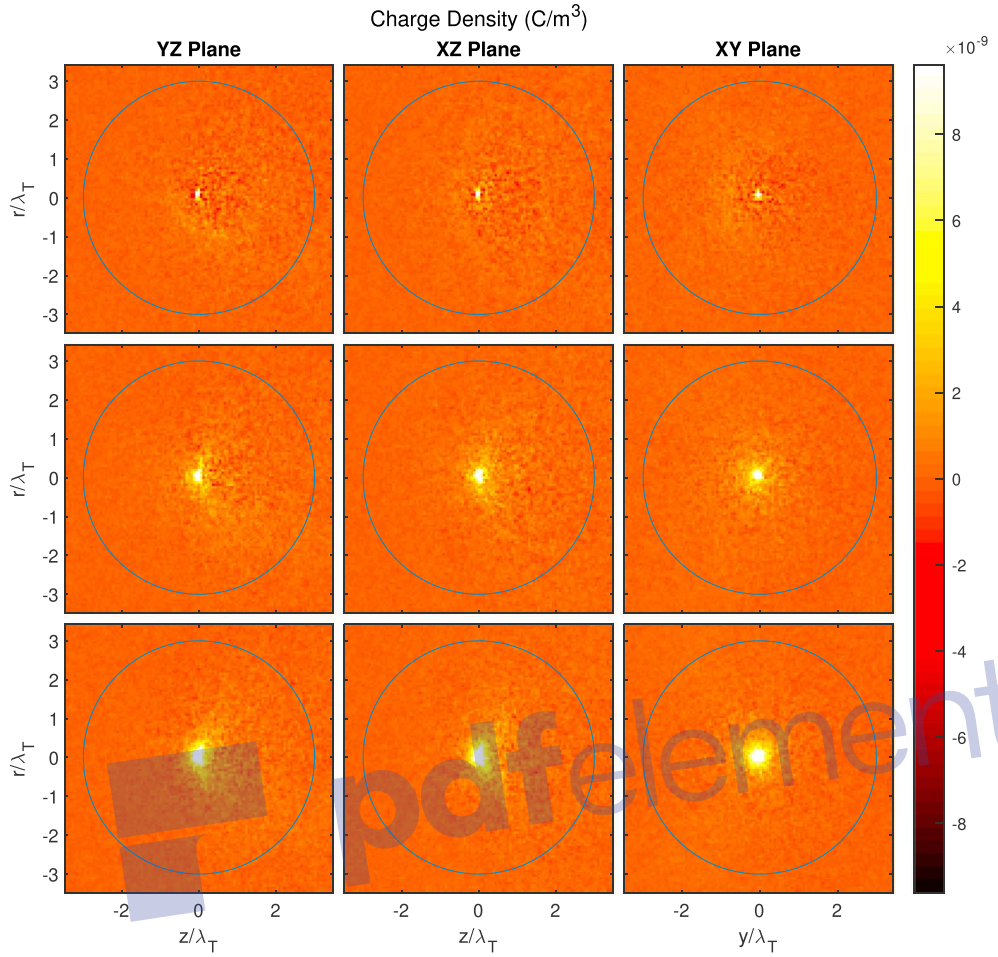

Figure 7. The charge density in coulombs per cubic meter in the *yz* (left column), *xz* (middle column), and *xy* column (right column) for the 1- (top row), 5- (middle row), and 10-eV (bottom row) electron model simulations. The near-meteoroid range is inside the blue circle.

(left column), *xz*, (middle column), and *xy* (right column) planes for the three different simulations (1 eV on the top row, 5 eV on the middle row, and 10 eV on the bottom row). The Figure 6 plots show that a changing electron energy model has no noticeable effect on the ion distributions but a significant effect on the electron distributions in the near-meteoroid region: As the electron energy increases, the electron density decreases for $r/\lambda_T < 1$. Because the ion density remains relatively constant between the simulations, the reduced electron density in the near-meteoroid region creates a pocket of positive charge density that can be seen in Figure 7. As the electron energy increases, the positive charge density region becomes larger.

The charge imbalance causes a positive potential that peaks at the meteoroid center and extends out of the near-meteoroid region and can be seen in Figure 8, a plot of the potential along the meteor path for the three different electron energy simulations. The potential difference between the center of the meteoroid and where the meteoroid path crosses the BP_+ boundary for the 1-, 5-, and 10-eV simulations is 0.39, 1.17, and 1.58 V, respectively, while the potential difference between the meteoroid center and where the meteoroid path crosses the BP_ boundary is 0.71, 1.93, and 2.19 V, respectively. For each simulation, the electron thermal energy is larger than the peak potential difference between the meteoroid center and either the front or back boundaries. This allows significant numbers of electrons to escape the potential well and contribute to the charge imbalance in the near-meteoroid region. Also, as the electron energy increases, the ratio of peak potential difference to electron energy decreases. This means that as the electron energy increases, a higher percentage of electrons will escape the near-meteoroid region resulting in a larger charge imbalance.

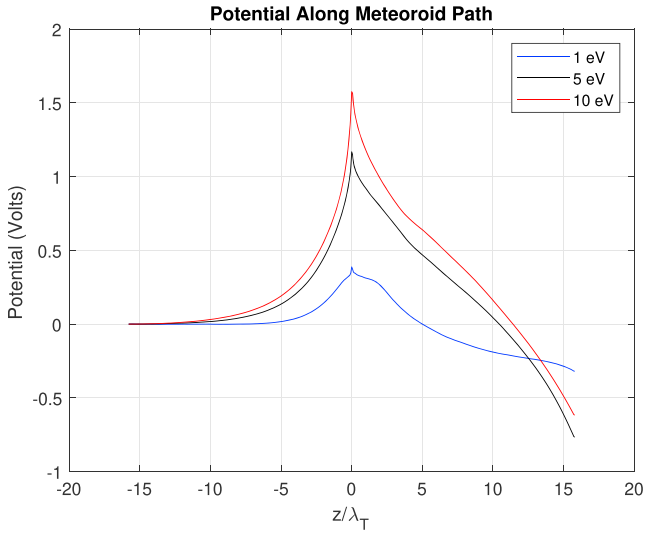

Figure 8. The potential along the meteor path for simulations with different electron energies. The 1-, 5-, and 10-eV results are in blue, black, and red, respectively.

There are two factors that could contribute to the charge imbalance. The first is that the high-velocity electrons move away from the meteoroid faster than the ions. The second is that the electrons are magnetized and the ions are not (the electron gyroradius is much smaller than their mean free path, while the ion gyroradius is much larger than their mean free path), and the background electric field due to the Lorentz transform causes magnetized particles to $\vec{E} \times \vec{B}$ drift behind the meteor. Therefore, electrons $\vec{E} \times \vec{B}$ drift while ions do not, further contributing to the charge imbalance near the meteoroid. The former seems to have more impact than the latter since the $\vec{E} \times \vec{B}$ drift is equal across the three simulations, while the electron energy (i.e., thermal velocity) varies. Figures 6 and 7 show that the region of electron depletion increases as the electron thermal velocity increases. Also, the electron depletion region in the yz and xz planes is roughly circular and centered on the origin. If the $\vec{E} \times \vec{B}$ drift were the main cause of the charge imbalance, we would expect the positive charge region to be elongated and shifted in the $\hat{z}$ direction.

3.5. Magnetic Field

We run four simulations to investigate the effects of a background magnetic field on the plasma. All four use the parameters in Table 1 except for the orientation and magnitude of $\vec{B}$. The first simulation uses the magnetic field in Table 1 which is oriented perpendicular to the meteor path ($\vec{B} = B\hat{x}$), the second has the magnetic field pointed 45° to the meteor path with components along $\hat{x}$ and $\hat{z}$, the third has the magnetic field along $\hat{z}$ (parallel to the meteor path), and the fourth has no magnetic field ($\vec{B} = 0$). Figure 9 shows the ion (top row) and electron (bottom row)

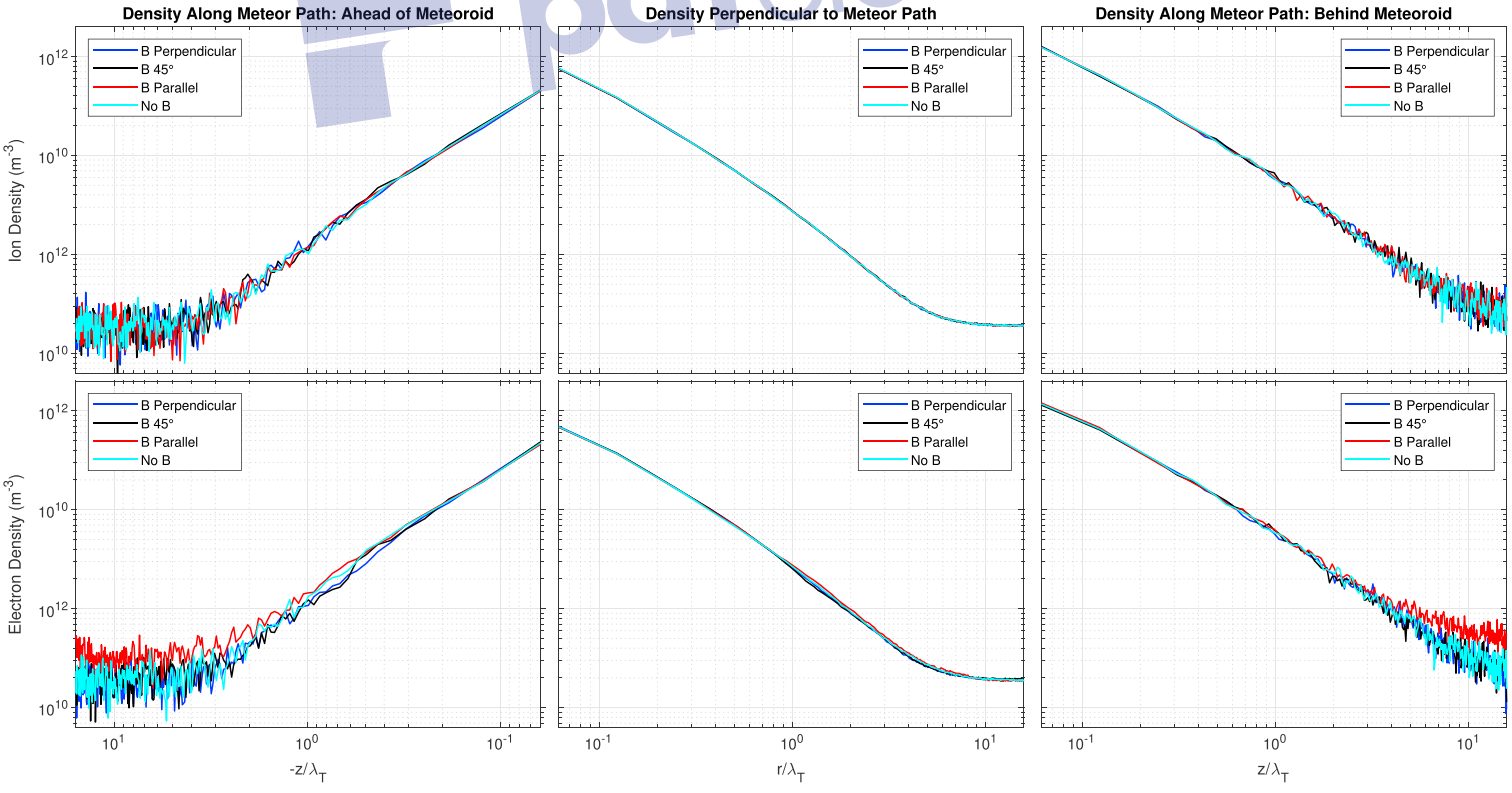

Figure 9. The ion (top row) and electron (bottom row) densities along four different contours for simulations with different background magnetic fields. The $\vec{B} \perp \hat{z}$, $\vec{B} \angle 45°$ $\hat{z}$, $\vec{B} \| \hat{z}$, and $\vec{B} = 0$ results are in blue, black, red, and cyan, respectively. The left plots show densities on a contour along the meteoroid path ahead of the meteoroid, the middle plots show densities on a contour perpendicular to the meteoroid path that passes through the meteoroid center, and the right plots show densities on a contour along the meteoroid path behind the meteoroid.

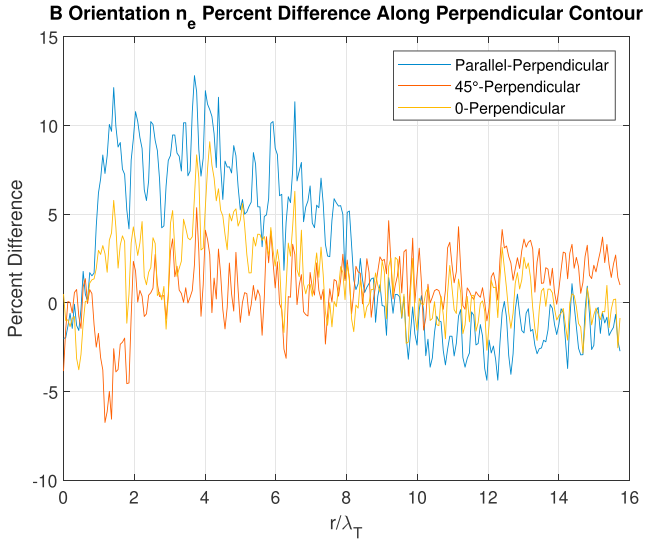

Figure 10. The n_e percent difference between the $\vec{B}||\hat{z}$-$\vec{B} \perp \hat{z}$ (blue), $\vec{B}\angle 45°\hat{z}$-$\vec{B} \perp \hat{z}$ (red), and $\vec{B} = 0$-$\vec{B} \perp \hat{z}$ (yellow) simulations along the perpendicular contour axially averaged about the meteor path.

densities along the usual contours for the four simulations. Similar to the field boundary conditions and electron energy models, the existence and orientation of $\vec{B}$ does not have a noticeable effect on the ion distribution. This makes sense because the ions are not magnetized. However, the electrons are magnetized and $\vec{B}$ does have an effect on the electron distributions. Figure 10 shows the electron density percent difference between the different $\vec{B}$ orientation simulations and the baseline simulation along the perpendicular contour.

There are two main differences in the electron distributions. The first is that the parallel $\vec{B}$ simulation has higher electron densities for contours along the meteor path in the far-meteoroid region than the other simulations (see bottom left and bottom right plots of Figure 9). This is likely due to a combination of magnetized electrons that are constrained to move along $\vec{B}$ and the lack of an external $\vec{E}$ from the Lorentz transformation for the parallel $\vec{B}$ simulation. The external $\vec{E}$ in the $\vec{B} \perp \hat{z}$ and $\vec{B}\angle 45°\hat{z}$ causes electrons to $\vec{E}\times\vec{B}$ drift and have their guiding centers move across magnetic field lines. Without the external $\vec{E}$, electron guiding centers are restricted to a single magnetic field line. The meteoroid surface is the largest source of electrons because that is where the ablated neutral density is the highest. Therefore, a high number of ionizing collisions that generate free electrons occur near the origin. The guiding center of these electrons are stuck to the magnetic field line along the z axis for the parallel $\vec{B}$ simulation, causing an elevated number of electrons along the meteoroid path compared to the other three simulations. Another way to explain this is that in the Earth's frame of reference, the meteoroid is moving along a single magnetic field line in the parallel $\vec{B}$ simulation and across multiple magnetic field lines in the $\vec{B} \perp \hat{z}$ and $\vec{B}\angle 45°\hat{z}$ simulations. The guiding centers of electrons created from ionizing collisions near the meteoroid center are restricted to a single field line rather than spread across multiple field lines for the $\vec{B} \perp \hat{z}$ and $\vec{B}\angle 45°\hat{z}$ simulations.

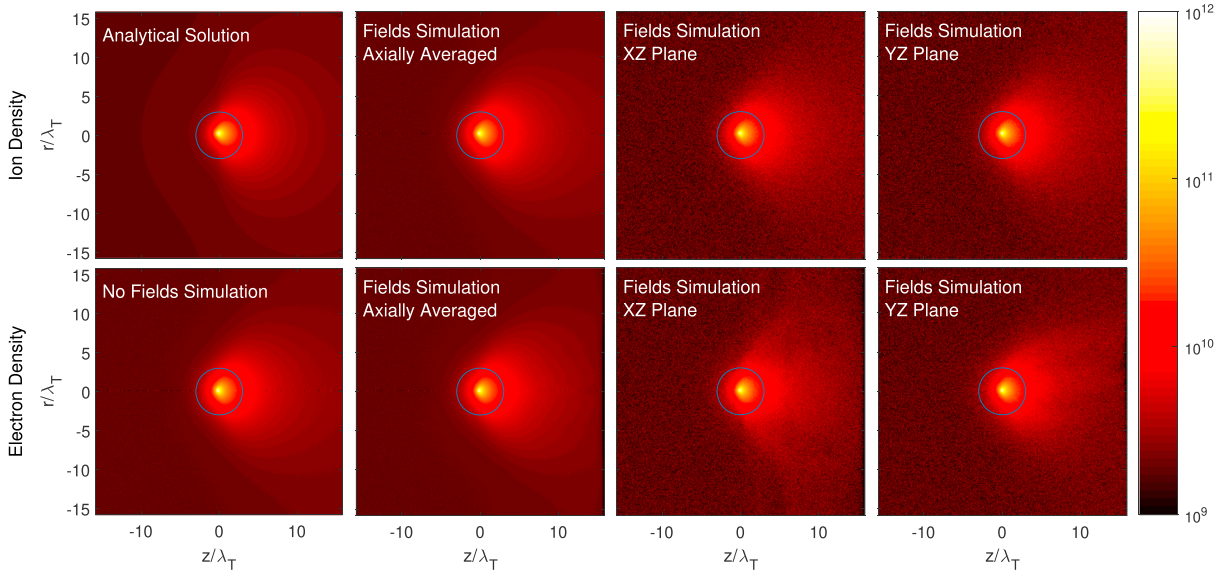

Figure 11. Ion (top row) and electron (bottom row) density distributions for the analytical solution, the simulations without electric or magnetic fields, and the simulation with electric and magnetic fields. The first column shows the plasma densities given by the DO analytical model on the top and the no-fields simulation results on the bottom. Note that the DO model and the no-fields simulation assume quasi-neutrality so the ion and electron densities are the same. The rest of the plots show data from the baseline simulation, that is, the simulation with electric and magnetic fields and Table 1 parameters. The second column shows the axially averaged density averaged about the meteoroid path for ions on the top and electrons on the bottom. The third column shows the particle densities in the xz plane containing the meteoroid center. The fourth column shows the particle densities in the yz plane containing the meteoroid center. The near-meteoroid region ($r/\lambda_T < 3$) is inside the blue circle. DO model = Dimant-Oppenheim model.

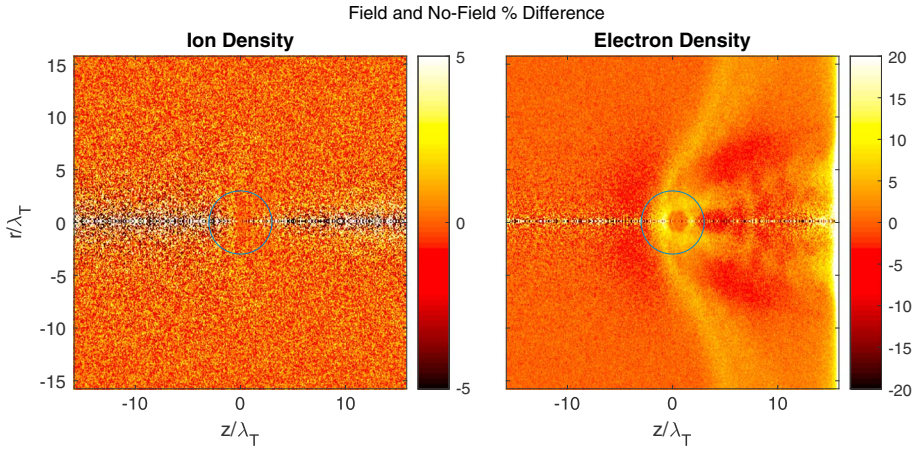

Figure 12. The percent difference of the axially averaged ion (left) and electron (right) densities between the no-fields and fields simulations with parameters in Table 1. The percent difference, PD, is calculated from $PD = 100(n_f - n_{nf})/n_f$, where n_f is the particle density for the fields simulation and n_{nf} is the particle density for the no-fields simulation. Since there are larger differences in the electron distribution, the electron plot's color ranges within ±20% and the ion plot's color ranges within just ±5%. The near-meteoroid region ($r/\lambda_T < 3$) is inside the blue circle.

The second major difference in electron distributions can be seen in Figure 10, where the percent difference between the $\vec{B}||\hat{z}$ and baseline simulation electron densities along the perpendicular contour between $1 < r/\lambda_T < 8$ is often above 5% and reaches a maximum of 12.8%. There is an even larger difference between the $\vec{B}||\hat{z}$ and $\vec{B}\angle 45°\hat{z}$ simulations with a maximum percent difference of 17.37% at $r/\lambda_T = 1.36$. We currently do not have an explanation for these differences, but they suggest it is important to take into consideration the effects of magnetic field orientation if using the electron distribution for modeling meteoroid mass from head echo RCS.

3.6. Comparison to Analytical Solution and No-Fields Simulation

The ion and electron density distributions for the simulation run with the Table 1 parameters (the "fields simulation"), the ion density distributions for the DO model, and a simulation run without electric or magnetic fields (the "no-fields" simulation) are shown in Figure 11. Because the DO model and the no-fields simulation are axially symmetric about the meteoroid path axis ($\hat{z}$) and assume quasi-neutrality, we axially average the ion densities (which are equivalent to electron densities because of quasi-neutrality) about $\hat{z}$. The results from the simulation with electric and magnetic fields are not axially symmetric, so we present the ion and electron densities on the xy plane and the yz plane that contain the meteoroid center. Despite the lack of axial symmetry in the "fields simulation", we also show the axially averaged ion and electron densities for comparison with the DO model and the no-fields simulation.

There are many interesting aspects to the results in Figure 11. The top row and the bottom left plot show that the ion densities of the DO model, no-fields simulation, and the fields simulation are remarkably similar, suggesting that the DO model's assumption that ion motion is not significantly affected by electric or magnetic fields is correct. The fields simulation's electron distribution is also similar to the DO model and no-fields simulation, but there is an axial asymmetry in the far-meteoroid region noticeable in the yz plane (bottom right plot). This asymmetry is likely due to the external $\vec{E} = -1.6\hat{y}$ V/m required to model the moving magnetic field lines. Even though the electrons are magnetized, they still experience collisions with atmospheric neutrals on a spatial scale longer than their gyroradius but smaller than the simulation domain. The net effect of collisions and the external electric field is a slight electron Pedersen drift in the $+\hat{y}$ direction, disrupting the axial symmetry of the DO model and the no-fields simulation.

Figure 12 shows the percent difference of the particle densities axially averaged about the meteor path between the no-fields simulation and the baseline field simulation. We show the axially averaged values because there is too much noise in the xz and yz plane cross sections. The top left highlights how the ion density distribution is hardly affected by the fields, with a maximum percent difference of $\sim$ 2% in the near-meteoroid region (ignoring the large fluctuations due to noise along $r = 0$). However, the right plot shows much larger electron differences, with a maximum difference of up to $\sim$ 20% in the

near-meteoroid region (again, ignoring the large fluctuations due to noise along $r = 0$). Also, the differences in the near-meteoroid ion densities do not have structure and appear to be mainly due to noise, while the near-meteoroid electron density differences have a clear structure.

4. Discussion and Conclusions

The simulations reported in this paper further develop the plasma density model for small meteors reported in Dimant and Oppenheim (2017a, 2017b) and numerically tested in Sugar et al. (2018) by investigating the effects of magnetic and electric fields. These simulations are the first published PIC simulations of a meteor head echo that include electric and magnetic fields and resolve all appropriate length and time scales. We validated the simulations by investigating the effects of boundary conditions, domain size, and electron energy models. The results show that the ion distribution is largely unaffected by the background magnetic field or electric fields generated by the plasma, while the electron distribution is affected by both magnetic and electric fields.

We examined how the electron distribution is affected by two parameters, the model used to assign electron energies after ionizing collisions and the background magnetic field orientation with respect to the meteor path. By varying the energies of electrons created via ionization, we showed a region of positive charge near the meteoroid that grows as the electron energies increase. We also showed that the $\vec{B}$ orientation effects the electron distribution in both the near- and far-meteoroid regions. There is a clear axial asymmetry when $\vec{B}$ is perpendicular to the meteor path.

Nevertheless, the fact that the reported ion distributions remain so similar to the no-fields simulations despite the different electron distributions is further evidence in support of the DO model's assumption that magnetic and electric fields have negligible impact on ion distribution. The simulations also support the results of Dimant and Oppenheim (2017a, 2017b) and Sugar et al. (2018) in that the plasma densities in the meteor head region are significantly different than the spherically symmetric Gaussian distributions used to estimate meteoroid mass from head echo observations.

A potential limitation of the PIC simulations presented in this work is that the meteoroid is assumed to be ablating solely Na atoms and all ions are Na^+. While it would be interesting to study the effects of multiple ion types, we restrict ourselves to a single ion for simplicity. The particular choice of Na has little effect on the simulations since we treat ionizing collisions as elastic due to the much higher collision energy than ionization energy. This is a reasonable assumption for other common elements found in meteoroids (Fe, K, Mg, and Si). We chose Na due to its bright presence in meteor spectra and its low mass which reduces the mean free path and λ_T (Ceplecha et al., 1998). Simulating a more massive element such as iron would increase the mean free path and would require more grid cells in order to fit the same number of λ_T inside the simulation because of the requirement to resolve the Debye length which would remain unchanged. Because the data are presented with the spatial coordinates normalized to λ_T, scaling the results for different elements and mean free paths is trivial.

We have not yet fully calculated how these new distributions will affect meteoroid mass estimates. However, Marshall et al. (2017) investigated five different spherically symmetric plasma distributions and found the meteoroid mass estimate could change by a factor of 3 depending on the choice of plasma distribution. Therefore, it is possible that the spherically asymmetric distribution given by the PIC simulations and the DO model will change mass estimates significantly. We are currently running Finite-Difference Time-Domain simulations to measure the RCS of plasma distributions derived from the PIC simulations and the DO model. This will enable a direct comparison of meteoroid mass estimates and the associated errors between these new plasma distributions and the spherically symmetric Gaussian distributions used in previous studies.

Acknowledgments
This work was supported by NSF grants AGS-1244842, AGS-1056042, and AGS-1755020. This work used the Extreme Science and Engineering Discovery Environment (XSEDE), which is supported by National Science Foundation grant ACI-1548562. The authors acknowledge the Texas Advanced Computing Center (TACC) at The University of Texas at Austin for providing HPC resources that have contributed to the research results reported within this paper (http://www.tacc.utexas.edu). The EPPIC simulation code and the input files used to generate the results are available at the website (https://gitlab.com/oppenheim_public/electrostatic_meteor_ablation_sim).

References

Berry, H. W. (1961). Energy distribution of electrons from ionizing collisions of heavy particles. *Physical Review*, *121*, 1714–1719. https://doi.org/10.1103/PhysRev.121.1714

Bouanich, J.-P. (1992). Site-site Lennard-Jones potential parameters for N_2, O_2, H_2, CO and CO_2. *Journal of Quantitative Spectroscopy & Radiative Transfer*, *47*, 243–250. https://doi.org/10.1016/0022-4073(92)90142-Q

Bret, A., & Dieckmann, M. E. (2010). How large can the electron to proton mass ratio be in particle-in-cell simulations of unstable systems? *Physics of Plasmas*, *17*(3), 32109. https://doi.org/10.1063/1.3357336

Bronshten, V. A. (1983). *Physics of meteoric phenomena*. Dordrecht/Boston/Lancaster: D. Reidel Publishing Company. https://doi.org/10.1007/978-94-009-7222-3

Campbell-Brown, M. D., Kero, J., Szasz, C., Pellinen-Wannberg, A., & Weryk, R. J. (2012). Photometric and ionization masses of meteors with simultaneous EISCAT UHF radar and intensified video observations. *Journal of Geophysical Research*, *117*, A09323. https://doi.org/10.1029/2012JA017800

Ceplecha, Z., Borovicka, J., Elford, W. G., Revelle, D. O., Hawkes, R. L., Porubcan, V., & Simek, M. (1998). Meteor phenomena and bodies. *Space Science Reviews*, *84*, 327–471. https://doi.org/10.1023/A:1005069928850

Chau, J. L., & Woodman, R. F. (2004). Observations of meteor-head echoes using the Jicamarca 50 MHz radar in interferometer mode. *Atmospheric Chemistry & Physics*, *4*, 511–521. https://doi.org/10.5194/acp-4-511-2004

Chulliat, A., Macmillan, S., Alken, P., Beggan, C., Nair, M., Hamilton, B., et al. (2015). The US/UK World Magnetic Model for 2015–2020: Technical report, National Geophysical Data Center, NOAA. https://doi.org/10.7289/V5TB14V7

Close, S., Brown, P., Campbell-Brown, M., Oppenheim, M., & Colestock, P. (2007). Meteor head echo radar data: Mass-velocity selection effects. *Icarus*, *186*, 547–556. https://doi.org/10.1016/j.icarus.2006.09.007

Close, S., Oppenheim, M., Durand, D., & Dyrud, L. (2005). A new method for determining meteoroid mass from head echo data. *Journal of Geophysical Research*, *110*, A09308. https://doi.org/10.1029/2004JA010950

Close, S., Oppenheim, M., Hunt, S., & Dyrud, L. (2002). Scattering characteristics of high-resolution meteor head echoes detected at multiple frequencies. *Journal of Geophysical Research*, *107*, 1295. https://doi.org/10.1029/2002JA009253

Dimant, Y. S., & Oppenheim, M. M. (2017a). Formation of plasma around a small meteoroid: 1. Kinetic theory. *Journal of Geophysical Research: Space Physics*, *122*, 4669–4696. https://doi.org/10.1002/2017JA023960

Dimant, Y. S., & Oppenheim, M. M. (2017b). Formation of plasma around a small meteoroid: 2. Implications for radar head echo. *Journal of Geophysical Research: Space Physics*, *122*, 4697–4711. https://doi.org/10.1002/2017JA023963

Dyrud, L., & Janches, D. (2008). Modeling the meteor head echo using Arecibo radar observations. *Journal of Atmospheric and Solar-Terrestrial Physics*, *70*, 1621–1632. https://doi.org/10.1016/j.jastp.2008.06.016

Frost, L. S., & Phelps, A. V. (1962). Rotational excitation and momentum transfer cross sections for electrons in H_2 and N_2 from transport coefficients. *Physical Review*, *127*, 1621–1633. https://doi.org/10.1103/PhysRev.127.1621

Janches, D., Nolan, M. C., Meisel, D. D., Mathews, J. D., Zhou, Q. H., & Moser, D. E. (2003). On the geocentric micrometeor velocity distribution. *Journal of Geophysical Research*, *108*, 1222. https://doi.org/10.1029/2002JA009789

Janches, D., & Revelle, D. O. (2005). Initial altitude of the micrometeor phenomenon: Comparison between Arecibo radar observations and theory. *Journal of Geophysical Research*, *110*, A08307. https://doi.org/10.1029/2005JA011022

Marshall, R. A., Brown, P., & Close, S. (2017). Plasma distributions in meteor head echoes and implications for radar cross section interpretation. *Planetary and Space Science*, *143*, 203–208. https://doi.org/10.1016/j.pss.2016.12.011

Oppenheim, M. M., & Dimant, Y. S. (2013). Kinetic simulations of 3-D Farley-Buneman turbulence and anomalous electron heating. *Journal of Geophysical Research: Space Physics*, *118*, 1306–1318. https://doi.org/10.1002/jgra.50196

Oppenheim, M. M., Dimant, Y., & Dyrud, L. P. (2008). Large-scale simulations of 2-D fully kinetic Farley-Buneman turbulence. *Annales Geophysicae*, *26*, 543–553. https://doi.org/10.5194/angeo-26-543-2008

Schunk, R. W., & Nagy, A. F. (2004). *Ionospheres*. Cambridge, UK: Cambridge University Press. https://doi.org/10.1017/CBO9780511635342

Sugar, G., Oppenheim, M. M., Dimant, Y. S., & Close, S. (2018). Formation of plasma around a small meteoroid: Simulation and theory. *Journal of Geophysical Research: Space Physics*, *123*, 4080–4093. https://doi.org/10.1002/2018JA025265

Towns, J., Cockerill, T., Dahan, M., Foster, I., Gaither, K., Grimshaw, A., et al. (2014). Xsede: Accelerating scientific discovery. *Computing in Science & Engineering*, *16*(5), 62–74. https://doi.org/10.1109/MCSE.2014.80

Vondrak, T., Plane, J. M. C., Broadley, S., & Janches, D. (2008). A chemical model of meteoric ablation. *Atmospheric Chemistry & Physics*, *8*, 7015–7031. https://doi.org/10.5194/acp-8-7015-2008

Zinn, J., Close, S., Colestock, P. L., MacDonell, A., & Loveland, R. (2011). Analysis of ALTAIR 1998 meteor radar data. *Journal of Geophysical Research*, *116*, A04312. https://doi.org/10.1029/2010JA015838